Proceedings 10th NUMGE 2023
10th European Conference on Numerical Methods in Geotechnical Engineering
Zdravkovic L, Kontoe S, Taborda DMG, Tsiampousi A (eds)

https://doi.org/10.53243/NUMGE2023-120

The anisotropic preconsolidation of clay in modelling soil-structure-interface behaviour

S. Gehring[1], A. Niemunis[1], H. H. Stutz[1]

[1]*Institute of Soil Mechanics and Rock Mechanics, Karlsruhe Institute of Technology, Karlsruhe, Germany*

ABSTRACT: Contact models can be derived from existing soil models, due to similar structure-soil-interface and soil behaviour. In this work, an anisotropic preconsolidation surface from the existing anisotropic visco-hypoplasticity model is used to evaluate asymptotic shear stresses reached through undrained contact shearing. The maximum shear stresses in different inclined contact shear planes are anisotropic due to preloading which renders the soil structure anisotropic. The preloading is memorized by a tensorial state variable. An example preloading path with oedometric condition is given and the evaluation of state variables is discussed. The influence of shear plane rotation, shear rate and surface roughness are investigated.

Keywords: induced anisotropy, preconsolidation surface, interface behaviour, fine grained soil, preloading history

1 INTRODUCTION

Most geotechnical projects deal not only with soil but include solid structures such as foundations, walls, piles etc. The interaction between soil and structure is often decisive, for example for skin friction piles or anchors. Therefore, especially the investigation of interface shearing is important to find satisfying solutions for geotechnical problems. This inspired many authors to laboratory tests and model experiments to examine the interface shear behaviour, for example Wernick (1978).

The structure-soil-interface behaves similarly to the adjacent soil. Many prevalent methods for contact modelling use established soil models for the derivation (Arnold & Herle, 2006; Staubach, et al., 2022; Stutz, et al., 2016).

The above-mentioned attempts for contact modelling are based on different assumptions concerning the stress state at the interface (Figure 4). While Arnold and Herle (2006) suppose all normal stresses to be equal ($T_{11} = T_{22} = T_{33}$) for simplicity, Stutz, Mašin, & Wuttke (2016) resign this. They assume the in-plane deformation to vanish and allow the in-plane stress to take other values than the stress normal to the interface ($T_{11} \neq T_{22} = T_{33}$). The approach of Staubach, Machaček, & Wichtmann (2022) couples neither the in-plane stresses nor the in-plane deformations directly with each other but with the neighboured soil (in FEM) so all normal stresses can be different ($T_{11} \neq T_{22} \neq T_{33}$).

For the modelling of soils loading path dependence and structure anisotropy are important. Instead of a direct dependence on the recent strain path most incremental constitutive models express loading history by some scalar or tensorial state variables. Tensorial state variables render the material description anisotropic – for example in the anisotropic visco-hypoplasticity model (Niemunis, et al., 2009).

By using tensorial state variables the contact behaviour can be rendered anisotropic similar to existing soil models. This is applied here by using the anisotropic preconsolidation surface of the existing anisotropic visco-hypoplasticity (AVHP model).

2 SIMPLIFIED ANISOTROPIC VISCO-HYPOPLASTICITY (BASED ON NIEMUNIS ET AL. (2009))

The use of symbols and notation is: Vectors and second-order tensors are marked with bold and italic typeface ($\boldsymbol{T}$), fourth order tensors by bold and not italic typeface ($\mathbf{E}$). The deviator of a tensor is marked with a star ($\boldsymbol{T}^*$).

The presented calculations are based on the anisotropic visco-hypoplasticity model (Niemunis, et al., 2009; Tafili, et al., 2023) for fine-grained soils. It is adopted for contact behaviour and partially used in a simplified way with reduced parameters. The Zaremba-Jauman terms for rigid body rotation are not considered here but would change the resulting stresses slightly. In the anisotropic visco-hypoplasticity the deformation is split into elastic, viscous (^{vis}) and hypoplastic (^{Hp}) portions:

$$\boldsymbol{T} = \boldsymbol{E}:(\boldsymbol{D} - \boldsymbol{D}^{vis} - \boldsymbol{D}^{Hp}) \tag{1}$$

$$\boldsymbol{D}^{vis} = \boldsymbol{m} D_r OCR^{-\frac{1}{I_v}} \quad and \quad \boldsymbol{D}^{Hp} = C_1 \boldsymbol{m} ||D|| \tag{2}$$

The hypoplastic strain $\boldsymbol{D}^{Hp}$ causes accumulation during strain cycles and is neglected for the evaluation of asymptotic states (Section 4, $C_1 = 0$). So the plastic strain is driven by the viscous portion $\boldsymbol{D}^{vis}$ dependent on the over consolidation ratio OCR, the flow rule $\boldsymbol{m}$ and material parameters.

In this model, a preconsolidation surface is defined to determine the over consolidation ratio and the flow rule. It is specified by two state variables: the structure tensor $\boldsymbol{\Omega}$ and the preconsolidation pressure p_B. The preconsolidation ellipse can be rendered anisotropic (e.g. by an anisotropic preloading) which deforms the

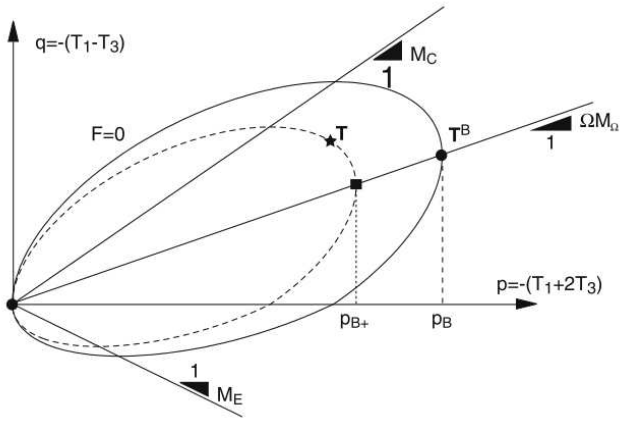

Figure 1. Preconsolidation surface (solid line) and scaled ellipse passing through the current stress $\boldsymbol{T}$ *(dashed line) (Niemunis, et al., 2009).*

ellipse. This is represented by the structure tensor $\boldsymbol{\Omega}$ while p_B scales the size of the ellipse. To evaluate the over consolidation ratio, the pressure p_B^+ is found scaling the preconsolidation ellipse, so it passes through the current stress state (see Figure 1) and the overconsolidation ratio becomes:

$$OCR = p_B/p_B^+ \tag{3}$$

A rate dependency is also considered by the viscous portion $\boldsymbol{D}^{vis}$: The deformation rate is related to the reference creep rate D_r taking also the viscosity index I_v and the current over consolidation pressure into account.

The used material parameters for this work are taken from (Niemunis, et al., 2009) and presented in Table 1.

3 STATE EVOLUTION

3.1 Stress state evolution during preloading

Many interface tests are conducted under oedometric conditions (e.g. (Boukpeti & White, 2017; Martinez & Stutz, 2019; Lemos & Vaughan, 2000)). In this section, a reasonable starting stress state for an interface shear test is evaluated by applying a preloading step. The exemplary preloading takes place under oedometric conditions (no radial deformation), a vertical

Table 1. Material parameters of kaolin clay for the anisotropic visco-hypoplastic model (Niemunis, et al., 2009)

e_{100}	$\boldsymbol{\lambda}$	$\boldsymbol{\kappa}$	$\boldsymbol{I_v}$	$\boldsymbol{D_r}$
0.94	0.09	0.025	0.031	1.3 10^{-6}/s
$\boldsymbol{\varphi_c}$	$\boldsymbol{C_1}$	$\boldsymbol{C_2}$	$\boldsymbol{C_3}$	
20°	0.09	0.025	0.031	

deformation ten times faster than the reference creep rate was applied. Figure 2 shows the evolution of the void ratio and the stresses during axial deformation.

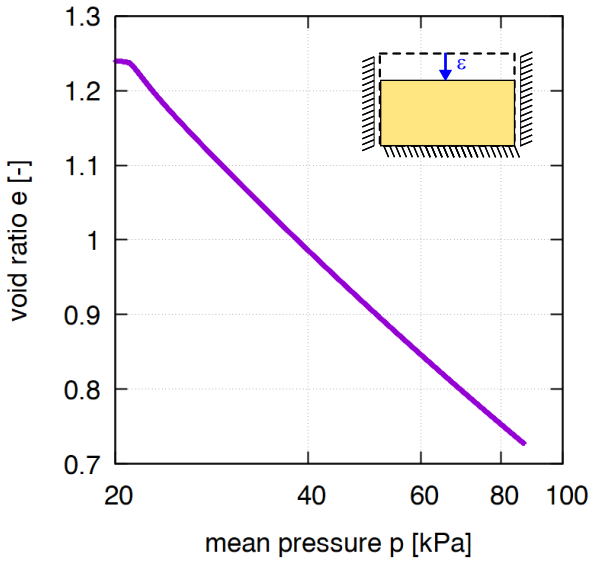

Figure 2. Evolution of void ratio and mean pressure during preloading.

After preloading, the following stress state $\boldsymbol{T}$, structure tensor $\boldsymbol{\Omega}$ and preloading pressure p_B is reached:

$$\boldsymbol{T} = \begin{bmatrix} -110 & 0 & 0 \\ 0 & 75 & 0 \\ 0 & 0 & 75 \end{bmatrix}, \boldsymbol{\Omega} = \begin{bmatrix} -0.22 & 0 & 0 \\ 0 & 0.11 & 0 \\ 0 & 0 & 0.11 \end{bmatrix}$$

$$p_B = 85\ kPa$$

Figure 3 presents the evaluation of the normal stresses and the components of $\boldsymbol{\Omega}$ during preloading. The values of $\boldsymbol{\Omega}$ reaches a plateau after approximately five per cent of deformation.

As the axial symmetric conditions indicate, the resulting stress state is axial symmetric (symmetry axis x_1'), but not isotropic: a lower value for the radial stresses than the axial stress is reached. The structure tensor $\boldsymbol{\Omega}$ also shows an axial symmetry. Note, that the trace of $\boldsymbol{\Omega}$ will vanish.

Based on this starting point the possible asymptotic states for an undrained shearing in a plane orthogonal to

the symmetry axis x_1' and in other directions are evaluated in Section 4.

3.2 Stress state evolution during simple shearing

During interface shearing, different types of deformation can occur contrary to simple shearing in a continuum. Assuming there is no significant discontinuity ($u_s \approx 0$ in Figure 4) in the continuum, soil shearing will only cause shear deformation γ in the soil. Regarding interface-soil-contacts, sliding and friction should be possible, allowing a strong discontinuity between the solid surface and the soil (Uesugi & Kishida, 1986). Therefore, the deformation of the interface can be split into a sliding displacement u_s and a displacement u_γ due to shear deformation (see Figure 4).

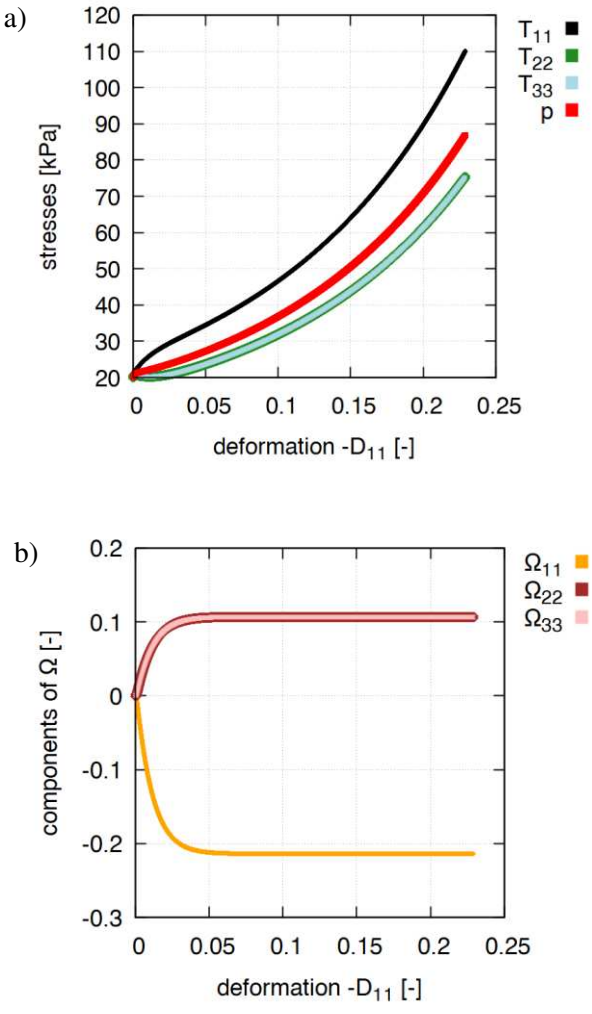

Figure 3. Evaluation of normal stresses (a) and the components of $\boldsymbol{\Omega}$ (b) during preloading

In this work, we take a simplification and consider only the shear deformation γ without splitting the relative displacement into a sliding and a friction part. Some authors consider the additional displacement by a virtual thickness of the shear band which is evaluated by back calculations (Arnold, 2008).

Concerning the evolution of stress state on interfaces, two different approaches for interface modelling were already mentioned in Section 1. Arnold & Herle (2006) assume all normal stresses take the same value ($T_{11} = T_{22} = T_{33}$), Stutz, Mašin, & Wuttke (2016) included another degree of freedom by allowing the in-plane stresses to be different from the interface normal stress ($T_{11} \neq T_{22} = T_{33}$).

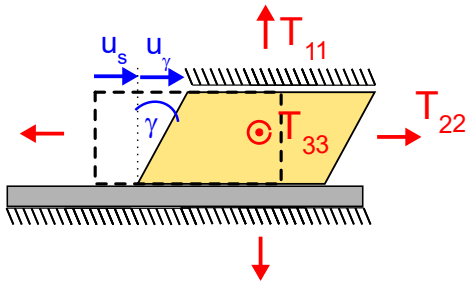

Figure 4. Sliding and friction on interfaces

Depending on the flow rule, the asymptotic state reached after long shearing (critical state) will have equal normal stresses: To reach an asymptotic state, the stress state has to vanish ($\dot{\boldsymbol{T}} = \mathbf{0}$). For models with a splitting of the deformation in an elastic and other portions, an applied deformation of pure shearing (Equation 4) has to be equal to the plastic strain (following from Equation 5):

$$\boldsymbol{D} = \begin{bmatrix} 0 & . & . \\ . & 0 & . \\ . & . & 0 \end{bmatrix} \tag{4}$$

$$\mathbf{0} = \dot{\boldsymbol{T}} = \boldsymbol{E} : (\boldsymbol{D} - \boldsymbol{D}^{vis}) \tag{5}$$

And for the simplified anisotropic visco-hypoplasticity holds:

$$\boldsymbol{D} = \boldsymbol{D}^{vis} = \boldsymbol{m} D_r OCR^{-\frac{1}{I_v}} \tag{6}$$

As Equation 6 indicates, $\boldsymbol{m}$ is proportional to the applied strain $\mathbf{D}$. Following these relations, we assume a pure deviatoric and radial flow rule in the asymptotic state. Radial in this case means radial to the hydrostatic axis in the stress space. Presupposing coaxiality between the flow rule $\boldsymbol{m}$ and the deviator of the current stress tensor $\boldsymbol{T}$ in the critical state, the stress tensor reaches the following form at the asymptotic state with equal normal stresses:

$$\boldsymbol{T} = \begin{bmatrix} p & \tau_{12} & \tau_{13} \\ \tau_{12} & p & 0 \\ \tau_{13} & 0 & p \end{bmatrix} \tag{7}$$

For this form of the stress tensor, the Lode angle takes the value $\theta = 30°$. This behaviour can be found in different constitutive models for the critical state as simulations from Medicus et al. (2022) with the clay

hypoplasticity (Mašín, 2013) show (note the different definition of Lode angle $\theta = 0°$ there). The behavior can differ for other relations between the current stress and the flow rule.

As discussed in (Medicus, et al., 2022), existing DEM simulations support the findings of a Lode angle $\theta = 30°$ at the critical state (Thornton & Zhang, 2006; Bernhardt-Barry et al., 2021) however DEM results of (Wijewickreme, et al., 2013) are contrary.

3.3 Evolution of state variables during shearing

The structure tensor $\boldsymbol{\Omega}$ and the preconsolidation pressure p_B are important state variables for the simplified anisotropic visco-hypoplasticity. They define the preconsolidation surface and include the anisotropic structure of the material e.g. after anisotropic preconsolidation (see Section 2).

As defined by the model, the structure tensor $\boldsymbol{\Omega}$ and the preconsolidation pressure p_B cannot change during undrained conditions ($\mathrm{tr}[\boldsymbol{D}] = 0$), they only change when $\mathrm{tr}[\boldsymbol{D}] < 0$ holds.

The values of the structure tensor $\boldsymbol{\Omega}$ and the preconsolidation pressure p_B in the asymptotic state after an undrained shearing are equal to the values at the beginning of the stage. These values can be transferred from the results of the example preloading stage in Section 3.1.

4 ASYMPTOTIC STATES FOR UNDRAINED SHEARING

The asymptotic state for shearing lies on the intersection between the failure criterion (here Matsuoka-Nakai is used) and the scaled preconsolidation ellipse corresponding to the current stress tensor (see Figure 5).

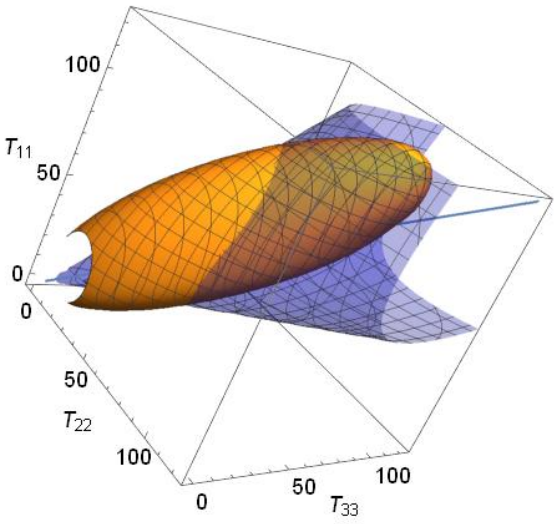

Figure 5. Preconsolidation surface (orange) and Matsuoka-Nakai criterion (blue). The intersection marks possible asymptotic states.

In the following, it is assumed that all normal stresses have the same value in the asymptotic state as declared in Section 3.2 for coaxiality between the stress tensor and the flow rule, as well as a purely deviatoric and radial flow rule at the critical state. Due to this assumption, a unique solution for the maximum shear stresses in the shearing plane reached on the asymptotic state can be found:

$$\textit{Matsuoka-Nakai: } F_{MN} = \frac{3}{2}\boldsymbol{T}^*:\boldsymbol{T}^* - M^2p^2 = 0 \qquad (8)$$

Preconsolidation surface:

$$F_B = M^2p^2 - 3Mp\,\boldsymbol{T}^*:\boldsymbol{\Omega} + \frac{3}{2}\boldsymbol{T}^*:\boldsymbol{T}^* + M\sqrt{\frac{3}{2}\boldsymbol{T}^*:\boldsymbol{T}^*}\,p_B\left(\frac{3}{2}\boldsymbol{\Omega}:\boldsymbol{\Omega} - 1\right) = 0 \qquad (9)$$

The combination of these two equations leads to the following form, representing the intersection of the Matsuoka-Nakai-criterion and the preconsolidation surface:

$$F_x = 3\,\boldsymbol{T}^*:\boldsymbol{T}^* + \sqrt{\frac{3}{2}\boldsymbol{T}^*:\boldsymbol{T}^*}\left(M\,p_B\left(\frac{3}{2}\boldsymbol{\Omega}:\boldsymbol{\Omega} - 1\right) - 3(\boldsymbol{T}^*:\boldsymbol{\Omega})\right) \qquad (10)$$

Pairs of shear stresses (τ_1, τ_2) which satisfy this equation are possible asymptotic states.

4.1 Shear plane rotation

Based on the structure tensor $\boldsymbol{\Omega}$ and the preconsolidation pressure p_B resulting from the preloading from Section 3.1 the asymptotic states for shearing in shear planes with different inclinations were evaluated with a shear deformation rate corresponding to the reference creep rate and a rough surface ($k_r = 1$, see Section 4.3).

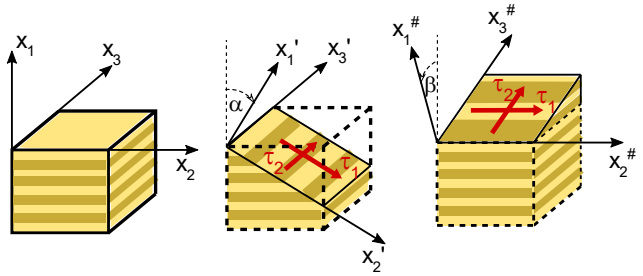

Figure 6. Coordinate system of shear plane. Left: Shear plane orthogonal to preconsolidation axis. Center: Rotation around the x_3-axis. Right: Rotation around the x_2-axis.

Figure 6 explains the different positions of the shear planes for the evaluated asymptotic shear stresses τ_1 and τ_2. On the left, the origin coordinate system with the x_1-axis parallel to the direction of the preconsolidation deformation is displayed. The rotation with angle α around the x_3-axis is shown in the centre and results in the coordinate system x_i'. For rotation

with the angle β around the x_2-axis, the coordinate system $x_i^{\#}$ is defined on the right.

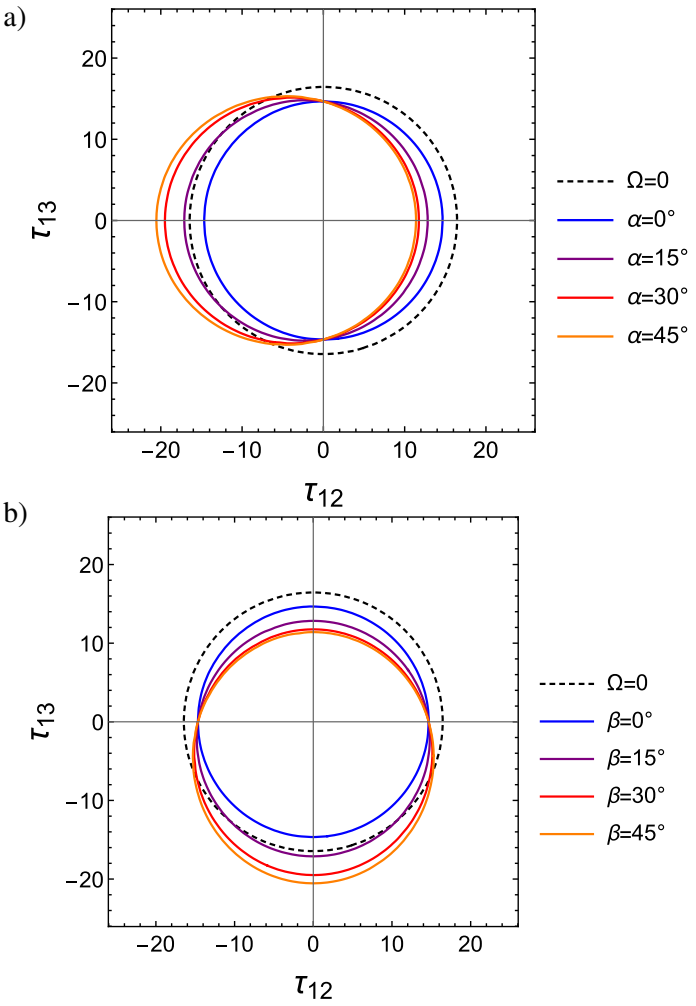

Figure 7. Contour of asymptotic shear stresses τ_{12} und τ_{13} corresponding to coordinate axes x_i' (a) and coordinate axes $x_i^{\#}$ (b) in Figure 6. Shear plane is rotated with α around the x_3-axis (a) or with β around the x_2-axis (b) of coordinate system x_i coaxial to preloading planes.

As a reference, the asymptotic shear stresses for a not anisotropic rendered preconsolidation surface (structure tensor $\boldsymbol{\Omega} = \mathbf{0}$) are displayed in Figure 7 in dashed lines besides the asymptotic states after anisotropic preloading for shear planes with different inclinations.

The rotation of the shear plane with angle α results in anisotropic maximum shear stresses with different values not only for the different shear axis τ_1 and τ_2. A shift of the centre of the intersection ellipse occurs resulting in different maximum shear stress along one axis in the positive or negative direction. A similar behaviour is shown for rotation with β (see Figure 7 b)) but the effects are swapped for the shear axes.

To give an example of the consequences of changed values of the structure tensor $\boldsymbol{\Omega}$, the contours of asymptotic shear stress states for another $\boldsymbol{\Omega}$ with doubled values are presented in Figure 8. With greater $\boldsymbol{\Omega}$, the scaling of the asymptotic state ellipse is more pronounced. Different values for the structure tensor $\boldsymbol{\Omega}$ can appear due to different preloading conditions, for example radial deformation $\neq 0$.

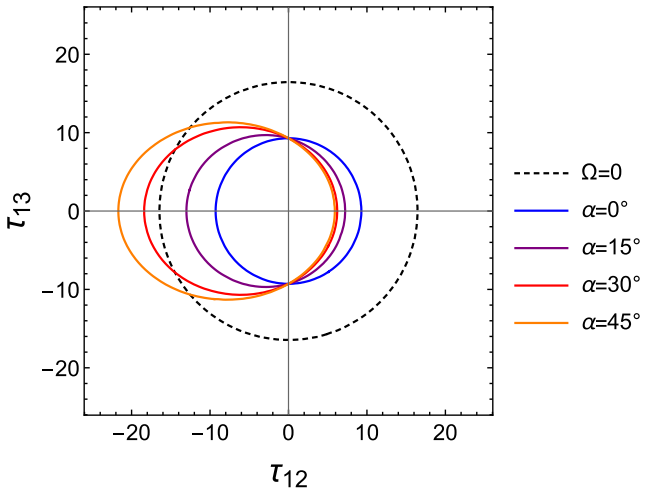

Figure 8. Contour of asymptotic shear stresses τ_{12} and τ_{13} corresponding to coordinate axes x_i in Figure 6 (center) for another $\Omega = 2 * \Omega_1$. Shear plane is rotated with α around the x_2-axis of coordinate system x_i coaxial to preloading planes.*

4.2 Rate dependence

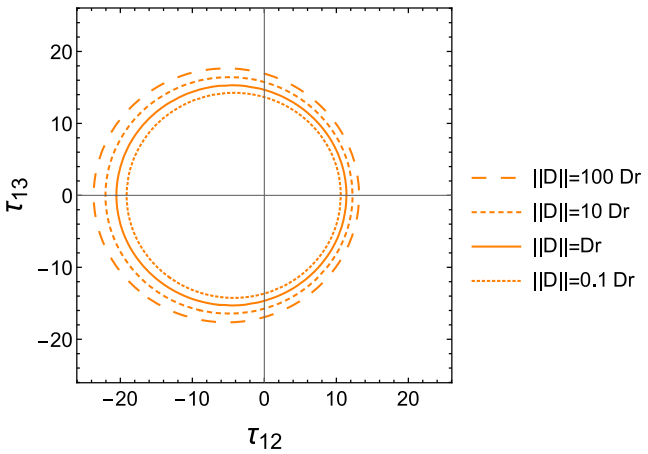

Figure 9. Contour of asymptotic shear stresses τ_{12} and τ_{13} for different shear deformation rates corresponding to coordinate axes x_1' in Figure 6 (center) with $\alpha = 45°$.

The rate dependence of the simplified anisotropic hypoplasticity is controlled by the reference creep rate D_r (see Section 2). With faster shearing greater values for the shear stresses are reached. This becomes visible for the contour of possible asymptotic shear stresses (see Figure 9) exemplary for a shear plane with rotation angel $\alpha = 45°$.

4.3 Surface roughness

In the previous sections, a rough contact in the shear plane was assumed. To take the surface roughness into account, the parameter k_r is used, characterizing the roughness with values between 1 (totally rough) and 0 (totally smooth, no friction mobilized) following e.g.

Arnold and Herle (2006). The critical stress ratio $M = q/p$ is now reduced and evaluated dependent on the reduced friction angle, $k_r\,\varphi$. Therefore, the maximum shear stresses reach lower values, as shown in Figure 10.

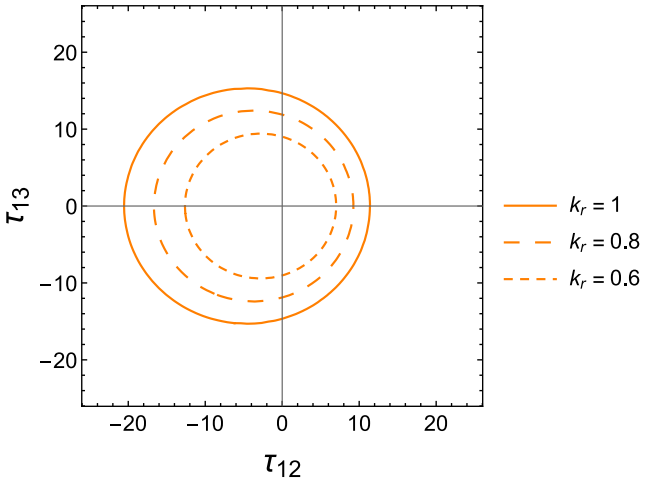

Figure 10. Contour of asymptotic shear stresses τ_{12} and τ_{13} for different surface roughness with parameter k_r corresponding to coordinate axes x_I' in Figure 6 (centre) with $\alpha = 45°$.

5 CONCLUSIONS

The anisotropic visco-hypoplasticity (Niemunis, et al., 2009) was used to first evaluate the evolution of state variables during an oedometric preloading of an interface. The preloading leads to an anisotropic stress state and renders the structure tensor **Ω** to a plateau value.

Based on the starting point of this preloading, the anisotropic preconsolidation surface and the Matsuoka-Nakai-criterion were used to evaluate the asymptotic state of maximum shear stresses reached during undrained interface shearing.

The rotation of the shear plane with respect to the preconsolidation axes leads to anisotropic asymptotic shear stresses with different values for the different axes on the plane as well as shearing in negative and positive direction. This behaviour retains for different shear rates and surface roughness. As expected, lower shear rates and lower surface roughness result in lower maximum shear stresses.

For the modelling of geotechnical problems including solid structures like foundations, anchors or piles, the interface behaviour is important for the resulting deformations. The consideration of the here shown anisotropic rendering of the soil during preloading will alter the maximum shear stresses and therefore the conclusions on the investigated projects. Experiments for comparison with the theoretical findings are presented in (Niemunis et.al., 2023).

6 REFERENCES

Arnold, M. 2008. Application of the Intergranular Strain Concept to the Hypoplastic Modelling of Non-Adhesive Interfaces. *The 12th International Conference of INternational Association for Computer Methods and Advances in Geomechanics (IACMAG),* Goa, India

Arnold, M., Herle, I. 2006. Hypoplastic description of the frictional behaviour of contacts. *Numerical Methods in Geotechnical Engineering,* 101–106. Taylor & Francis, Graz, Austria.

Bernhardt-Barry, M. L., Biscontin, G., O'Sullivan, C. 2021. Analysis of the stress distribution in a laminar direct simple shear device and implications for test data interpretation. *Granular Matter* **23**, 1–17.

Boukpeti, N., White, D. J. 2017. Interface shear box tests for assessing axial pipe-soil resistance, *Géotechnique* **67**, 18–30.

Lemos, L. J. L., Vaughan, P. R. 2000. Clay-interface shear resistance, *Géotechnique* **50**, 55–64.

Martinez, A., Stutz, H. H. 2019. Rate effects on the interface shear behaviour of normally and overconsolidated clay, *Géotechnique*, **69**, 801–815.

Mašín, D., 2013. Clay hypoplasticity with explicitly defined asymptotic states, *Acta Geotechnica*, **8**, 481–496.

Medicus, G., Kwa, K., Cerfontaine, B. 2022. A consistent calibration process for the Matsuoka-Nakai friction angle under direct simple shear conditions for clay hypoplasticity, *Computers and Geotechnics*, **150**, 104888.

Niemunis, A., Grandas-Tavera, C. E., Prada-Sarmiento, L. F. 2009. Anisotropic visco-hypoplasticity, *Acta Geotechnica*, **4**, 293–314.

Niemunis, A., Gehring, S., Stutz, H. H. 2023. The undrained anisotropic strength of soil-structure interfaces in clay, *to be submitted*.

Staubach, P., Machaček, J., Wichtmann, T. 2022. Novel approach to apply existing constitutive soil models to the modelling of interfaces, *International Journal for Numerical and Analytical Methods in Geomechanics*, **46**, 1241–1271.

Stutz, H., Mašin, D., Wuttke, F. 2016. Enhancement of a hypoplastic model for granular soil–structure, *Acta Geotechnica*, **11**, 1249–1261.

Tafili, M., Gehring, S., Knittel, L., Wichtmann, T.; Stutz, H. H. 2023. An experimental and numerical study on the influence of inherent and induced anisotropy of a fine-grained soil, *Soils and Foundations. submitted*.

Thornton, C., Zhang, L. 2006. A numerical examination of shear banding and simple shear non-coaxial flow rules, *Philosophical Magazine*, **86**, 3425–3452.

Uesugi, M. & Kishida, H., 1986. Frictional resistance at yield between dry sand and mild steel. *Soils and foundations*, **26**, 139–149.

Wernick, E. 1978. *Heft Nr. 75: Tragfähigkeit zylindrischer Anker in Sand unter besonderer Berücksichtigung des Dilatanzverhaltens.* Institute of Soil mechanics and Rock mechanics.

Wijewickreme, D., Dabeet, A., Byrne, P. 2013. Some observations on the state of stress in the direct simple shear test using 3D discrete element analysis, *Geotechnical Testing Journal*, **36**, 292–299.